

ON THE MASS DISTRIBUTION OF THE INTRA-CLUSTER LIGHT IN GALAXY GROUPS AND CLUSTERS

E. CONTINI^{1,2} AND Q. GU^{1,2}

¹School of Astronomy and Space Science, Nanjing University, Nanjing 210093, China; emanuele.contini82@gmail.com, qsgu@nju.edu.cn

²Key Laboratory of Modern Astronomy and Astrophysics (Nanjing University), Ministry of Education, China

ABSTRACT

We take advantage of a semi-analytic model with a state-of-art implementation of the formation of the intra-cluster light (ICL) to study the mass distribution of the ICL in galaxy groups and clusters, at different redshifts. We assume the ICL to follow a NFW profile with a different concentration, linked to that of the dark matter by the relation $c_{ICL} = \gamma c_{DM}$, where the parameter γ is set to reproduce the observed relation between the stellar mass in the brightest cluster galaxy (BCG) and ICL in the innermost 100 kpc and the halo mass ($M_{100}^* - M_{500}$), at $z = 0$. The model is then tested against several theoretical and observational results, from the present time to $z \sim 1.5$. Our analysis shows that the fraction of stellar mass in the BCG and ICL within the innermost 100 kpc is an increasing function of redshift, parameter γ , and a decreasing function of the halo mass. The value of γ required to match the observed $M_{100}^* - M_{500}$ is $\gamma = 3$ at $z = 0$, but there are hints that it might be a function of redshift and halo mass. This result indicates that the distribution of the ICL is more concentrated than the dark matter one, but less concentrated than previously found by other studies. We suggest that a modified version of the NFW is a good description of the distribution of the diffuse light in groups and clusters, which makes the ICL a reliable tracer of the dark matter, in good agreement with recent observational findings.

Keywords: galaxies: evolution - galaxy: formation.

1. INTRODUCTION

The intracluster light (ICL), which was first discovered by Zwicky (1937), is a diffuse component in galaxy groups and clusters made of stars that are not bound to any galaxy. It is commonly associated with the diffuse envelope of the most massive galaxies that reside in the center of groups and clusters (e.g., Gonzalez et al. 2013; Kravtsov et al. 2018), although a modest fraction has been found (e.g. Presotto et al. 2014) and predicted (e.g., Contini et al. 2018) to be around intermediate/massive satellites, especially in the most massive clusters in the local universe. Since its discovery, the ICL has been studied with the idea that it could shed some light on the processes at play in the formation of the large structures such as galaxy clusters.

In the last decade or so, many attempts, both from the observational and theoretical sides, have been made in order to understand the physical mechanisms that bring to the formation of the ICL (Murante et al. 2007; Purcell et al. 2007; Puchwein et al. 2010; Rudick et al. 2011; Contini et al. 2014; DeMaio et al. 2015; Burke et al. 2015; Iodice et al. 2017; Groenewald et al. 2017; Morishita et al. 2017; Tang et al. 2018; Montes & Trujillo 2018; DeMaio

et al. 2018; Contini et al. 2018; Montes & Trujillo 2019; DeMaio et al. 2020; Iodice et al. 2020 and many others). Most of this diffuse light is found around the brightest cluster galaxy (BCG) and so, as a natural consequence, the main mechanisms invoked to explain the formation of this component are those related to the formation and evolution of the BCGs, such as galaxy mergers and stellar stripping. From a theoretical point of view, the mutual role of these two processes would bring to different properties of both BCGs and ICL, such as colors and metallicity (a detailed discussion of this topic can be found in Contini et al. 2018, 2019).

Taking advantage of the latest version of the original model (presented in Contini et al. 2014) for the formation of the ICL, in Contini et al. (2018) we focused on the growth of the BCG and the ICL. Among the most relevant results obtained, we showed that BCGs and ICL form and grow at different times and with different rates (overall), but the two components co-evolve after redshift $z \sim 0.7$. Stellar stripping is the most important process in our model that leads to the formation of the ICL, and, around 90% of the ICL coming from this channel is actually produced in the innermost 150 kpc from the halo center, with a significant halo-to-halo scatter that mostly depends on the halo mass, and so on its concentration

(e.g., Gao et al. 2004; Contini et al. 2012; Prada et al. 2012). This result opens to the idea that the ICL cannot be simply thought as an envelope of the galaxy at which it is associated, but rather a self-consistent component, because (by definition) its stars are not bound to any galaxy and it can be extended as far as hundreds kpc. To this, we must also add the amount of ICL formed around satellites galaxies during the so-called pre-processing (see Han et al. 2018), and the non-negligible part of it that is accreted during the growth of the group/cluster (see, e.g. Contini et al. 2014).

During the last years, some authors attempted to study the connection between the growth of the ICL and the growth of the BCG (see references above), and only very recently by looking at the relation between the stellar mass of BCG and ICL within a given aperture and the halo mass (e.g. Kravtsov et al. 2018; DeMaio et al. 2018; Pillepich et al. 2018; DeMaio et al. 2020). Kravtsov et al. (2018), with a limited samples of galaxy groups and clusters in the local universe from X-ray observations, investigated the relation between the total stellar mass within a given aperture (what they call M_{BCG} , but it actually includes a significant part of the ICL) and the halo mass. They find a slope $\alpha = 0.4 \pm 0.1$, not far from 0.5, i.e. the value found by Gonzalez et al. (2013) (who considered the total stellar mass within the virial radius) and 0.37 ± 0.05 found by DeMaio et al. (2018) with a sample of 23 groups and clusters at $z \sim 0.4$ and considering only the stellar mass within the innermost 100 kpc. Pillepich et al. (2018) used the IllustrisTNG project, which is a set of cosmological magneto-hydrodynamical simulations of galaxy formation that were performed by using the code AREPO (Springel 2010), that comprises about 4000 groups and clusters with halo mass larger than $10^{13} M_{\odot}$. They looked at the $M_* - M_{halo}$ relation at redshift $z = 0$ considering the stellar mass at different apertures: 30 kpc, 100 kpc and 2 times the radius the encloses half of the stellar mass. They found an increasing value of the slope α with increasing aperture that goes from 0.49 (30 kpc), 0.59 (100 kpc) and 0.74 ($2r_{half}^{stars}$), which appears slightly high compared to the previous ones. Lately, DeMaio et al. (2020), with the same sample used in DeMaio et al. (2018), found $\alpha = 0.48 \pm 0.06$ in the range $10 \text{ kpc} < r < 100 \text{ kpc}$.

The idea behind this paper is to assume a profile for the distribution of the ICL mass and, by using the aforementioned observed data to roughly set the model, compare our predictions against different observed and simulated properties of the BCG+ICL system. We will assume a modified version of the NFW profile (Navarro et al. 1997) to describe the distribution of the ICL mass in a halo. The ICL is mainly formed by stellar stripping of galaxies and mergers between them as they orbit around the center of the potential well of the cluster. By definition

of ICL, its stars are not bound to any galaxy but only to the potential well of the halo, and so is dark matter. It is reasonable to assume that the ICL would follow the gravitational potential in the same way (or similar to) dark matter does (see also Montes & Trujillo 2019).

We will take advantage of our model for the formation of the ICL (latest version described in Contini et al. 2019). A semi-analytic model does not provide any spatial information regarding the distribution of stars in galaxies. In order to have such information, we will assume a profile for the distribution of the ICL mass such that we can obtain the amount of stellar mass in ICL at any clustercentric distance. The parameter space of the profile will be tested against the available observational data and the prediction of the model compared with a plethora of recent simulated/observed radial distributions of BCG/ICL mass.

The paper is organized as follows. In Section 2 we briefly describe our model and the profile used to distribute the ICL mass in haloes. In Section 3 we present our analysis, which will be fully discussed in Section 4, and in Section 5 we summarize our main conclusions. Throughout this paper we use a standard cosmology, namely: $\Omega_{\lambda} = 0.76$, $\Omega_m = 0.24$, $\Omega_b = 0.04$, $h = 0.72$, $n_s = 0.96$ and $\sigma_8 = 0.8$. Stellar masses are computed with the assumption of a Chabrier (2003) Initial Mass Function (IMF), and all units are h corrected. In the rest of the paper we refer to R_{200} and R_{500} (depending on the particular results we are comparing our predictions to) as the radii that enclose a mean density of 200/500 times the critical density of the Universe at the redshift of interest, and similarly for the masses enclosed to them, M_{200} and M_{500} .

2. METHODS

We take advantage of the semi-analytic model developed in Contini et al. (2014), which is a modified version of the one described in De Lucia & Blaizot (2007), and that considers different mechanisms for the formation and evolution of the ICL, mainly stellar stripping and galaxy mergers. The full prescription has been further improved in Contini et al. (2018) and Contini et al. (2019), so we refer the reader to these papers for the detail of the modelling, while below we provide a summary of the main features and assumptions.

2.1. General Features of the Semi-Analytic Model

The semi-analytic model ran on the mergers trees of a set of high-resolution N-body simulations whose details are provided in Contini et al. (2012) and Contini et al. (2014). The set comprises 27 zoom-in cluster simulations whose data have been stored at 93 output times, spanning a redshifts range between $z = 60$ and the present day, by using the cosmology reported in Section

1. At $z = 0$ our sample counts 361 groups and clusters with M_{200} larger than $10^{13} M_{\odot}/h$ and up to more than $10^{15} M_{\odot}/h$. Given the fact the mass of each dark matter particle is $10^8 M_{\odot}/h$, we resolve the largest clusters with more than 10 million particles.

To identify subhaloes within main haloes, we took advantage of the algorithm SUBFIND (Springel et al. 2001). This algorithm decomposes each FOF group into a set of different substructures that are identified as local overdensities in the field of the background halo. Similarly to previous works, where we used the same set of simulations, we considered as genuine subhaloes only those that could retain at least 20 bound particles. SUBFIND has been found to have some difficulties in accurately recover subhaloes particles when they are very close to the halo centre (see, e.g., Muldrew et al. 2011), which in principle can affect the predictions of the amount of ICL. However, our prescription for the formation of the ICL (see below in this section for a detailed discussion) acts almost entirely on galaxies for which their subhaloes went under the resolution of the simulation (20 particles), so that we do not expect this limitation of SUBFIND to influence the amount of ICL formed. Nevertheless, altering the number of bound particles required for a subhalo to be considered a genuine one and/or altering the mass resolution (higher/lower particle mass) do have an effect on the amount of ICL formed, simply because it affects the number of galaxies allowed to experience stellar stripping. For quantitative and qualitative details on this point we refer the reader to Contini et al. (2014), where the issue has been fully discussed in a dedicated appendix.

The semi-analytic model populated subhaloes with galaxies by means of several physical mechanisms that describe our current knowledge of galaxy formation and evolution, and by using the information on dark matter stored in the trees. Among all, the model includes the treatment of gas cooling, star formation, SN and AGN feedback, and the formation of the ICL which is the most important prescription in the context of this paper.

To implement the formation of the ICL we use the model named "Tidal Radius" in Contini et al. (2014), which operates on satellite galaxies, both with and without dark matter component. For each satellite, the semi-analytic model derives a tidal radius, R_t , which depends on the mass of the galaxy itself, the mass of the main halo, and the distance between the galaxy and the center of the halo where the BCG is positioned. Every galaxy, including satellites, is assumed to be a two-component system with a spheroidal bulge and an exponential disk. If the tidal radius R_t is small enough to be contained within the bulge, we assume the satellite galaxy to be disrupted and all its stellar mass moved to the ICL component associated with the BCG. If the tidal radius R_t is

larger than the bulge radius but smaller than the disk radius R_{sat} , we assume that the mass in the shell $R_t - R_{sat}$ is stripped and added to the ICL component of the BCG.

The implementation just described is directly applied to "orphan" galaxies, i.e. satellites that have lost their dark matter component (or it went under the resolution of the simulation), while for satellites with a dark matter component there is an extra requirement: we impose that the half mass radius of the dark matter subhalo that contains the satellite has to be smaller than the half mass radius of the disk component before stellar stripping can start. The Tidal Radius Model considers only the stripping of material while satellites are orbiting around the potential well of the cluster. The semi-analytic model allows for another channel for the formation of the ICL and it is provided by mergers, both minor and major. At each merger between a satellite and a central galaxy, 20% of the stellar mass of the satellite is moved to the ICL component associated with the central, and the rest added to its stellar mass (the reason of the percentage chosen is explained in Contini et al. 2014).

Other two important assumptions must be noted and concern the amount of ICL that central galaxies, i.e. BCGs included, can acquire in a non-direct way from satellite galaxies. Once a satellite with a dark matter component experiences the first episode of stripping, we assume that its ICL component is accreted to the ICL component associated with the current central galaxy. Similarly, once satellites become orphans or are accreted into larger haloes, their ICL component (if any) is moved to the ICL component of the current central galaxy. In both cases the ICL has been already formed and we usually refer to these processes as pre-processing, in the sense that the ICL formed somewhere else and then accreted by the central galaxy.

2.2. ICL Profile

For the purpose of our study, we need to model the mass distribution of the ICL. The main reason for that is given by the fact that a semi-analytic model does not provide any spatial information but the position of the galaxies (or others such as bulge/disk radii). A semi-analytic model is conceptually different from a hydrodynamical simulation, which works with particles that can be followed one by one. In order to describe the spatial distribution of the stars that constitute the ICL, we assume a modified version of the NFW profile. As anticipated in Section 1, such a profile is a reasonable assumption considering that the stars belonging to the ICL are not bound to any galaxy but only to the potential well of the cluster and so, like dark matter particles, they can be considered as a collisionless system. A similar argument has been recently discussed in Montes & Trujillo (2019) (but see also Alonso Asensio et al. 2020;

Kluge et al. 2020).

The NFW profile reads as follow:

$$\rho(r) = \frac{\rho_0}{\frac{r}{R_s} \left(1 + \frac{r}{R_s}\right)^2}, \quad (1)$$

where ρ_0 is the characteristic density of the halo at the time of its collapse and R_s is its scale radius, i.e. the radius at which the slope of the profile ($\log(\rho)$) is equal to -2. Once the scale radius is linked to the virial radius R_{200} , it is possible to define the concentration of the halo as

$$c = \frac{R_{200}}{R_s}. \quad (2)$$

We modify the classic profile described in Equation 1 by introducing a new parameter in Equation 2. Basically, we define the ICL concentration as

$$c_{ICL} = \gamma \frac{R_{200}}{R_s}. \quad (3)$$

The new parameter γ could be, in principle, a function of several halo properties and/or redshift. For the sake of simplicity, we will consider this parameter to be halo and redshift independent, but we will show our results by testing several values. Under this assumption, γ is then a multiplicative factor which acts on the concentration of the dark matter halo and returns the concentration of the ICL mass distribution. Considering the baryonic nature of the ICL, the channels of its formation and evolution, it is likely that the ICL is more concentrated than the dark matter halo, which translates in $\gamma > 1$. This is supported by several recent theoretical works (e.g. Contini et al. 2018; Pillepich et al. 2018) and observational studies (e.g. Montes & Trujillo 2019).

In the next section we will test the ICL profile described by Equations 1 and 3. The new profile allows us to know the ICL mass within any radial bin, which means that we can overplot our predictions on observational (and theoretical) results to test the validity of the profile itself, by varying the value of γ . We will focus in particular on the BCG+ICL mass within 100 kpc at different redshifts, and after having set the values of γ (we remind the reader that γ can be a function of redshift or some halo properties), we will test our predictions on several other observed and simulated quantities.

3. RESULTS

For the purposes of our analysis, we apply the model described in Section 2.2 at three redshifts, namely: $z=0$, 0.5, 1.5. Before going to the detail of the analysis, in Figure 1 we show the ratio between the mass in ICL and BCG contained within 100 kpc¹ from the center of

¹ In this paper we do not go below 100 kpc, and consider the mass of the BCG to be fully contained within that distance from the halo center.

Table 1. Intercepts and slopes with scatters of the $M_{100}^* - M_{500}$ relation (Figure 2) at the redshifts investigated, for $\gamma = 3$ and $\gamma = 5$. Data points have been fitted with the simple linear fit $\log M_{100}^* = \alpha \log(M_{500}/2 \cdot 10^{14}) + \beta$.

z	β ($\gamma = 3$)	α ($\gamma = 3$)	β ($\gamma = 5$)	α ($\gamma = 5$)
0	11.91 ± 0.04	0.41 ± 0.04	12.00 ± 0.04	0.46 ± 0.04
0.5	11.67 ± 0.05	0.38 ± 0.05	11.74 ± 0.05	0.42 ± 0.05
1.5	11.53 ± 0.09	0.41 ± 0.09	11.57 ± 0.09	0.44 ± 0.09

the halo and the total ICL-BCG mass within R_{200} , as a function of the halo mass (which spans a wide range from $\log M_{200} \sim 13$ to $\log M_{200} \sim 15.3$), and at different redshifts (different colors) as shown in the legend. Each panel shows the prediction of the model for a particular value of the parameter γ , from $\gamma = 1$ (top left panel), to $\gamma = 6$ (bottom right panel). By focusing on any of the panels (i.e., independently of the value of γ), we can see that the the percentage of the mass in ICL and BCG in 100 kpc depends on both redshift and halo mass. The trend with redshift appears to be moderately strong, and so the trend with halo mass especially for higher values of γ .

Let's now consider an intermediate value of γ , such as $\gamma = 3$ (top right panel). In this particular case and at the present time, the percentage changes from 50% in the low halo mass end, to around 10% in the high halo mass end. If we consider the highest redshift, the change of the percentage is less dramatic, from $\sim 20\%$ to $< 10\%$, which means that the redshift increase is also halo mass dependent. Instead, by focusing on the different panels, it is possible to see another trend: the higher the value of γ , the higher the percentage of ICL and BCG mass within 100 kpc, regardless the halo mass, although the effect is certainly more evident toward lower halo masses. This trend can be easily explained by the fact that less massive haloes are more concentrated (and smaller) than more massive ones (Gao et al. 2004; Prada et al. 2012), together with the fact that haloes of a given mass are also, on average, less concentrated at higher redshift (e.g. Gao et al. 2011; Contini et al. 2012).

The key-point of this figure is that γ plays an important role and in the rest of the following analysis we set the model to the value that best fits the observations, according to the redshift of the observed data. We remind the reader that the parameter γ can be a function of halo mass, but can in principle be also a function of redshift, i.e. at different redshifts, different values of γ can be more appropriate.

Figure 2 shows the relation between the stellar mass of ICL and BCG within 100 kpc, and the mass M_{500} (hereafter $M_{100}^* - M_{500}$), for haloes at different redshift,

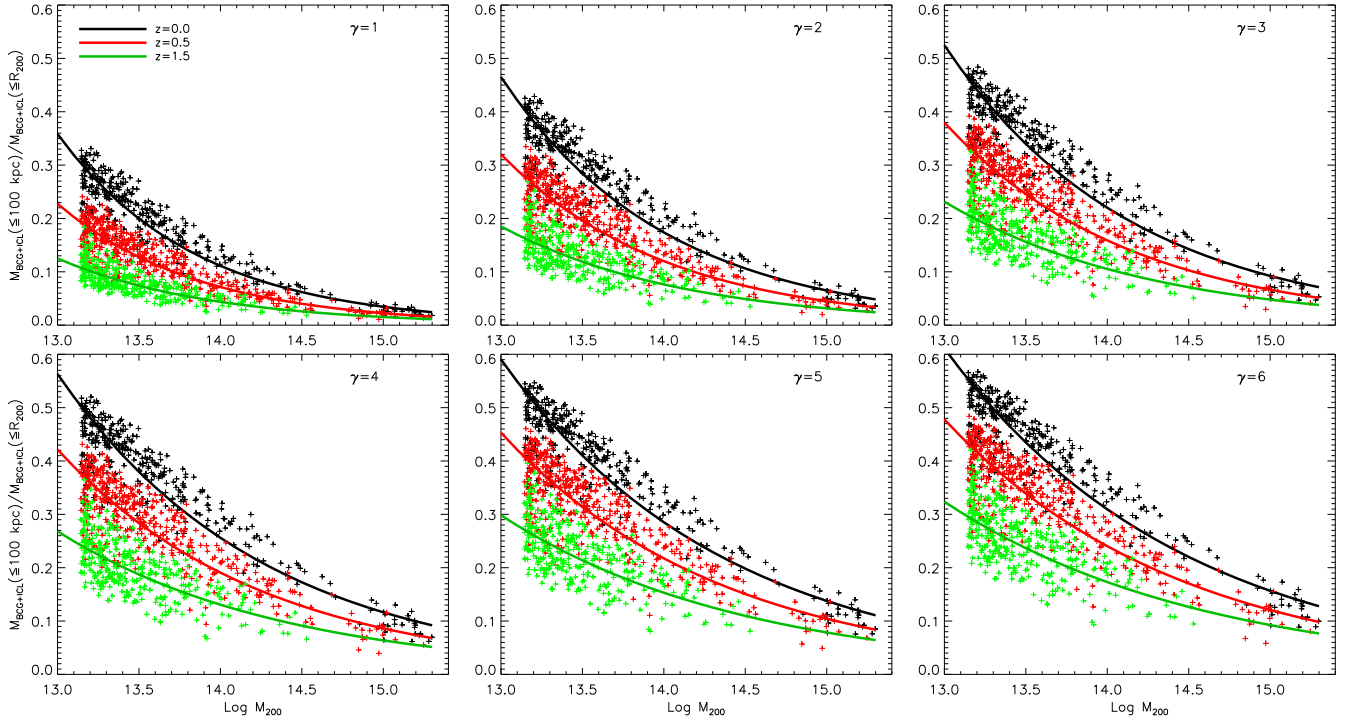


Figure 1. Ratios between the ICL-BCG mass within 100 kpc from the halo center and the total ICL-BCG mass within R_{200} , as a function of halo mass and at different redshifts as reported in the legend. Each panel shows the prediction of the model for a particular value of γ , which ranges from one to six. The percentage of the ICL-BCG mass enclosed in 100 kpc is an increasing function of redshift, (different colors), an increasing function of γ (different panels), and a decreasing function of halo mass. These trends are in line with the fact that less massive haloes are more concentrated and smaller than more massive ones, and with the fact that haloes of a given mass are, on average, less concentrated at higher redshift.

from $z = 0$ (top panels) to $z = 1.5$ (bottom panels). Our model predictions are compared with those of the IllustrisTNG simulations (Pillepich et al. 2018) at $z = 0$, and with the observed data by DeMaio et al. (2020) at all redshifts investigated (see legend). The two columns refer to the model predictions where we used $\gamma = 3$ (left column) and $\gamma = 5$ (right column). We have fit our data points with the simple linear fit

$$\log M_{100}^* = \alpha \log(M_{500}/2 \cdot 10^{14}) + \beta$$

and values of intercepts, slopes and scatter are reported in Table 1. Let's comment each panel of the figure. The first line of panels refers to the present time, and as for the others, the only difference between the two is given by the different values of γ (3 or 5) used. At redshift $z = 0$ our model (cyan lines and symbols) agrees well with the observational data (black symbols), and even better than the prediction of the IllustrisTNG simulation (blue line and symbols), by preferring a low value of γ . At redshift $z = 0.5$, although the model (red lines and symbols) reproduces well the slope of the the observational data (black lines and symbols), it is biased low with respect to them. What is possible to note at this redshift is that

observations suggest higher values of γ with respect to $z = 0$. The trend is confirmed at much higher redshift (bottom panels), where a simple linear fit (green lines) of our model predictions (green symbols) is able to match most of the observed data (black symbol). A possible reason for the bias seen at higher redshift can be the wide redshift range investigated in the work of DeMaio et al. (2020), where $z \sim 0.4/1.55$ are just the median of the redshift distributions. Another possible reason can be that the observed BCG or ICL masses are intrinsically different from those derived by the model². We will come back on this point in Section 4, while for the rest of our analysis we focus on the present time with the choice of $\gamma = 3$.

In Figure 3 we focus on the mass of ICL outside 100 kpc, and we plot it as a function of the mass M_{500} , at $z = 0$. Our model predictions (black lines) are compared with the result of Pillepich et al. (2018) (blue line and symbols). The trend found in the analysis of the IllustrisTNG data is reproduced, but our model predicts slightly higher amounts of ICL outside 100 kpc than

² A higher γ can transfer more ICL mass within 100 kpc. We ruled out this possibility by testing several extreme values.

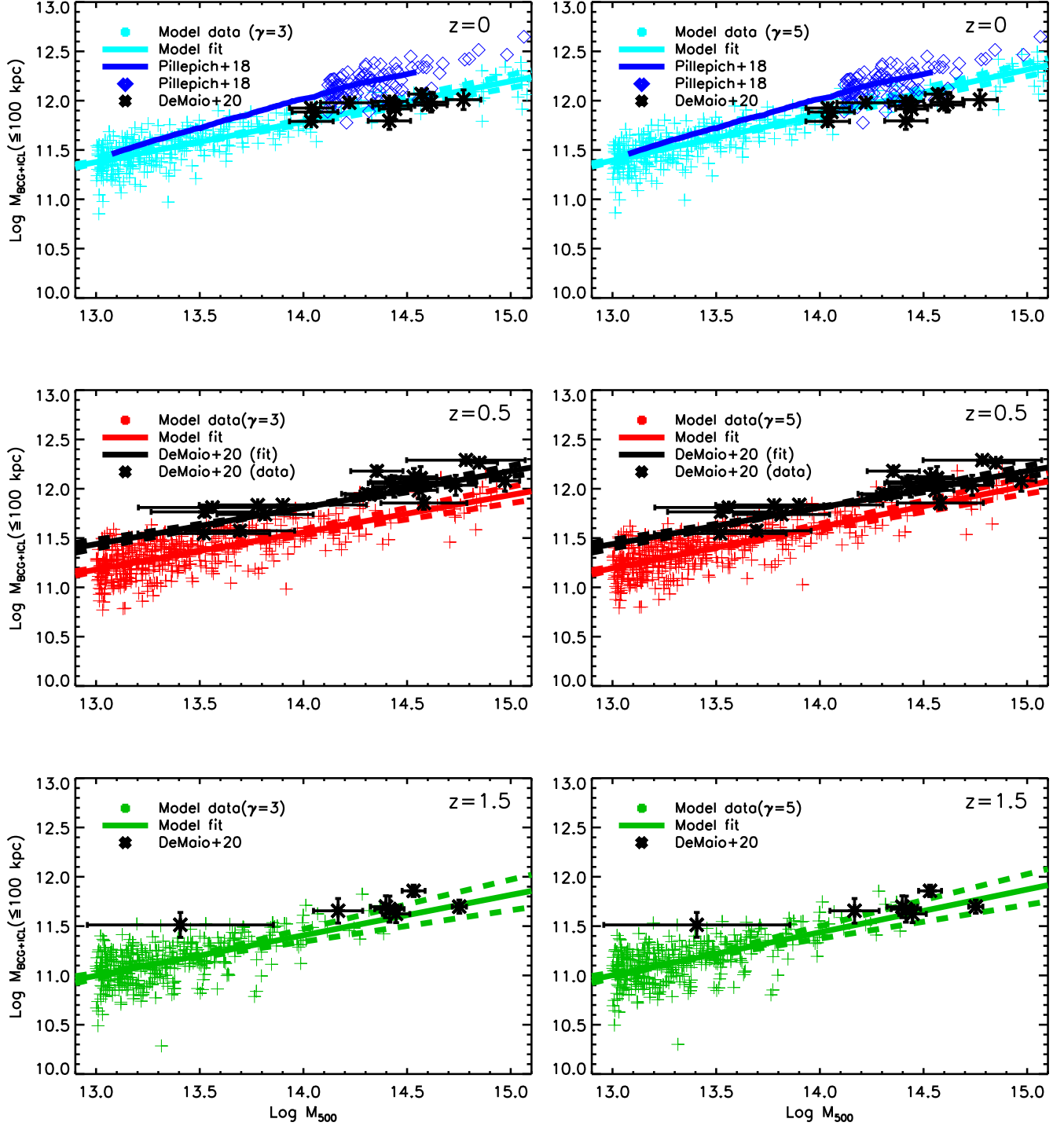


Figure 2. Relation between the ICL-BCG stellar mass enclosed in 100 kpc and the halo mass M_{500} , for groups and clusters at different redshifts as indicated in the legend. The two columns refer to the model predictions for $\gamma = 3$ (left column) and $\gamma = 5$ (right column). The model predictions are compared with the observed set of data by [DeMaio et al. \(2020\)](#) and the results of the IllustrisTNG simulations ([Pillepich et al. 2018](#)). Our model agrees well with the observed data in the local Universe and better than the prediction of the simulations by preferring low values of γ . At higher redshift it reproduces fairly well the observed trend and prefers higher values of γ . The values of the intercepts and slope of each fit are reported in Table 1.

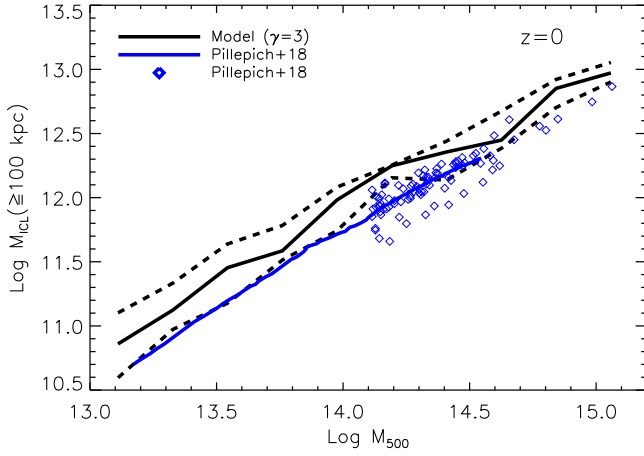


Figure 3. Mass of the ICL outside 100 kpc as a function of the halo mass M_{500} at $z = 0$ and $\gamma = 3$, compared with the results of Pillepich et al. (2018). Although the trend found by Pillepich et al. (2018) is reproduced, our model (black lines for median, 16th and 84th percentiles of the distribution) predicts slightly more ICL outside 100 kpc with respect to their simulation.

those predicted by the simulation. Roughly speaking, IllustrisTNG data are $1 - \sigma$ lower than our predictions. A caveat must be noted. Pillepich et al. (2018) call “central” all the stellar mass within a given distance from the center, and ICL the stellar mass outside that given distance (in this case 100 kpc). Our definitions of ICL are not fully comparable because we have made the assumption that the BCG is confined within 100 kpc, while in principle, in Pillepich et al. (2018), where no attempt to separate the two components is made, part of the BCG mass can extend farther than 100 kpc. The two definitions become the same in the case that no mass of their BCGs extends farther than 100 kpc. Further details on this will be given in Section 4. Moreover, another point must be clear: both here and in Pillepich et al. (2018) the assumption of spherical symmetry has been implicitly made and, as Pillepich et al. (2018) rightly state in their paper, it is a clear simplification.

In order to investigate on the possible causes of this difference, in Figure 4 we make a one-to-one comparison between our predictions and the result of the IllustrisTNG by looking at (from the top to the bottom): the mass of BCG+ICL within 100 kpc (top panel), the mass in ICL outside 100 kpc (central panel) over the total stellar mass within R_{200} , and the mass in ICL outside 100 kpc over the BCG+ICL mass within R_{200} (bottom panel), as a function of the mass M_{200} . The fraction of ICL and BCG mass within 100 kpc predicted by our model is lower with respect to the simulated data, at all halo masses. In the same halo mass range (from the low mass end to $\log M_{200} \sim 14.8$ of our sample), the fractions are 50% and 10% from our model, 65% and 20% from the

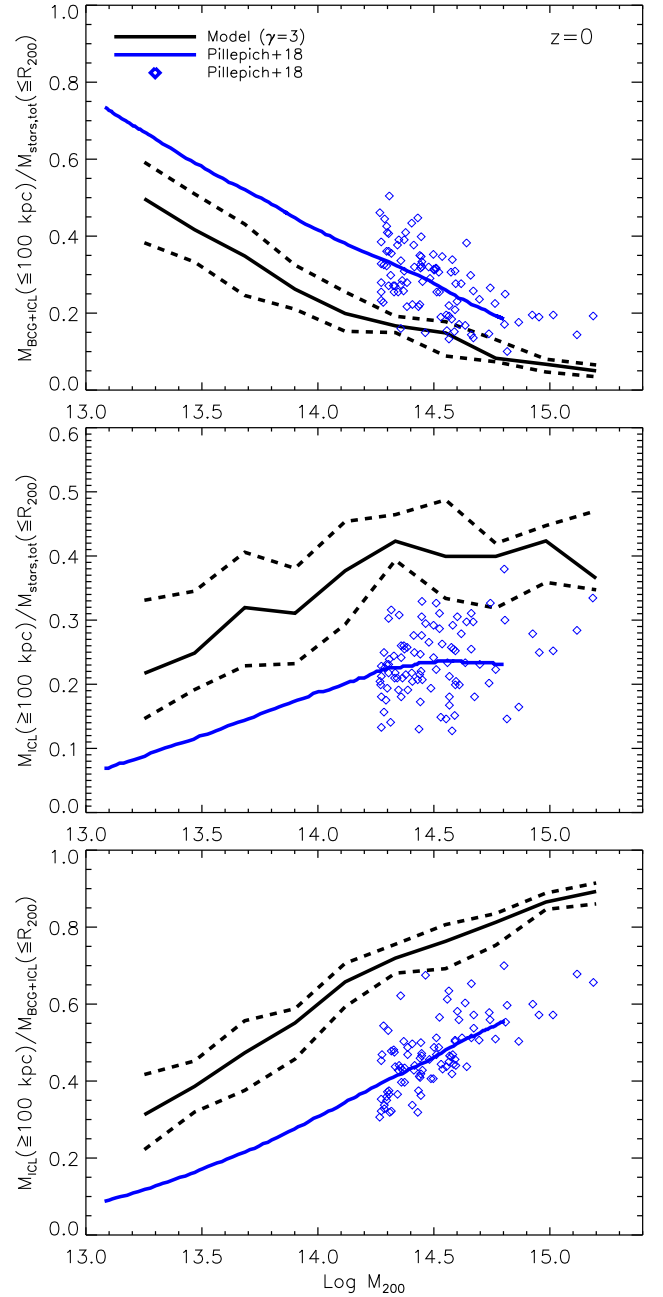


Figure 4. Different mass ratios as a function of the halo mass M_{200} . From top to bottom: the mass of BCG+ICL enclosed within 100 kpc (top panel), the mass in ICL outside 100 kpc (central panel) over the total stellar mass within R_{200} , and the mass in ICL outside 100 kpc over the BCG+ICL mass within R_{200} (bottom panel), as a function of the mass M_{200} . Our model predictions (black lines as in Figure 3) are compared with the predictions of the IllustrisTNG simulation (Pillepich et al. 2018). Compared to Pillepich et al. (2018), our model predicts a smaller fraction of BCG+ICL mass in the innermost 100 kpc, and a higher amount of ICL in the rest of a cluster (as seen in Figure 3).

simulation.

The central panel shows the complementary plot shown by the top panel, i.e. the mass of ICL outside 100 kpc normalized to the total stellar mass within R_{200} . This panel clearly shows that the trend is inverted with respect to the results found in the top panel, i.e. our model predicts higher fractions of ICL outside 100 kpc than IllustrisTNG. As noted above, the mismatch can be due to the different definitions of ICL used. However, assuming that the two definitions are comparable, there are two ways to explain the non-negligible difference in the results: (a) different amount of ICL predicted by our model if compared with IllustrisTNG or, (b) the ICL distribute differently in IllustrisTNG. We investigate further on this below. In the bottom panel of Figure 4 we plot the fraction of ICL outside 100 kpc over the total amount of BCG+ICL within R_{200} , as predicted by our model and by IllustrisTNG. Again, the two predictions are far from each other. In the halo mass range where they can be compared, our model goes from around 0.3 in low halo masses to 0.9 in the highest halo masses, while the fractions for IllustrisTNG are lower, 0.1 and 0.7 respectively.

In the left panel of Figure 5 we show the mass of BCG+ICL (black solid line), and the same with the contribution of satellite galaxies (black dash-dotted line), within R_{500} as a function of the halo mass M_{500} , and a detailed comparison with observed data from [Gonzalez et al. \(2013\)](#) and [Kravtsov et al. \(2018\)](#), and with IllustrisTNG ([Pillepich et al. 2018](#)) results. Interestingly, our predictions (whether we include satellites or not) are in perfect agreement with the results of IllustrisTNG, and also in good agreement with the observed data. Considering the precision with which our model and IllustrisTNG agree in this case, and considering what discussed above, this means that, although we both predict the same amount of BCG+ICL, the mass distributions of the ICL along the clusters are different. Our model, with respect to IllustrisTNG, predicts more ICL outside 100 kpc.

In order to double check the validity of our model, we plot in the right panel of Figure 5 the ratio within R_{500} between the BCG+ICL and total stellar mass as a function of the halo mass M_{500} , at redshift $z = 0$, and compare the model prediction (black lines) with the sets of data by [Gonzalez et al. \(2013\)](#) and [Kravtsov et al. \(2018\)](#), as indicated in the legend. Overall, the observed trend is reproduced although our results appear to be biased with respect to the cloud of the observed data. In particular, our predictions are closer to the green line, which refers to the results of [Kravtsov et al. \(2018\)](#) where, from a sample of haloes, stellar masses were assigned using stellar mass halo mass relation derived using an abundance matching technique and assuming a scatter of 0.2 dex.

However, for the quantities shown in both panels there are caveats which are worth discussing, and we will fully address them in Section 4.

In the next section we will discuss in detail the results presented in this section and, more important their consequences, in particular in light of the comparison with the observed data.

4. DISCUSSION

Our state-of-art model for the formation of the ICL is able to reproduce the total BCG+ICL mass within 100 kpc (this paper), as well as other important properties, as shown in former papers with detailed comparisons with observations. Given the semi-analytic nature of our model, it does not provide the spatial information of this component, i.e. how the ICL distributes along the cluster after it forms. We assumed a simple mass profile that links the distribution of the ICL to that of the dark matter, motivated by recent works such as [Montes & Trujillo \(2019\)](#), [Kluge et al. \(2020\)](#) and [Alonso Asensio et al. \(2020\)](#). The ICL mass profile is generalized from a NFW density profile of the dark matter, and the connection between the two profiles is given by the parameter γ introduced in Section 2.2 that links the two concentrations. This modelling of the ICL profile allows us to know, with the necessary information such as the ICL mass and virial radius of the cluster, the amount of ICL at any clustercentric distance (under the assumption of spherical symmetry).

We tested our model against the observed data by [DeMaio et al. \(2020\)](#) at different redshift and the simulated data at $z = 0$ from the IllustrisTNG simulation ([Pillepich et al. 2018](#)) by looking at the $M_{100}^* - M_{500}$ relation, where M_{100}^* is the total BCG+ICL mass within 100 kpc from the cluster center. Our profile is able to capture the slope of the relation from $z = 1.5$ to the present time, while the intercept at $z = 0.5$ seems to be lower than observed by around 0.2 dex. Overall, mild variations of γ do not considerably change the results, although our analysis suggests that γ might be an increasing function of redshift. In Section 3 we briefly discussed the gap at $z = 0.5$ between the observed and predicted intercepts as possibly due to the fact that while our relation is plotted exactly at that redshift, observed data span a wide redshift range around the median $z \sim 0.4$. It is, however, more likely that the BCG+ICL observed masses are intrinsically higher than those predicted by our model, which is in part caused by the intrinsic difficulty in detecting the full light and/or problems in separating the source from the sky, especially at higher redshift, and in part it might be due to the fact that the model slightly underestimates the total BCG+ICL mass with the same degree in the whole halo mass range investigated. We will come back on this below.

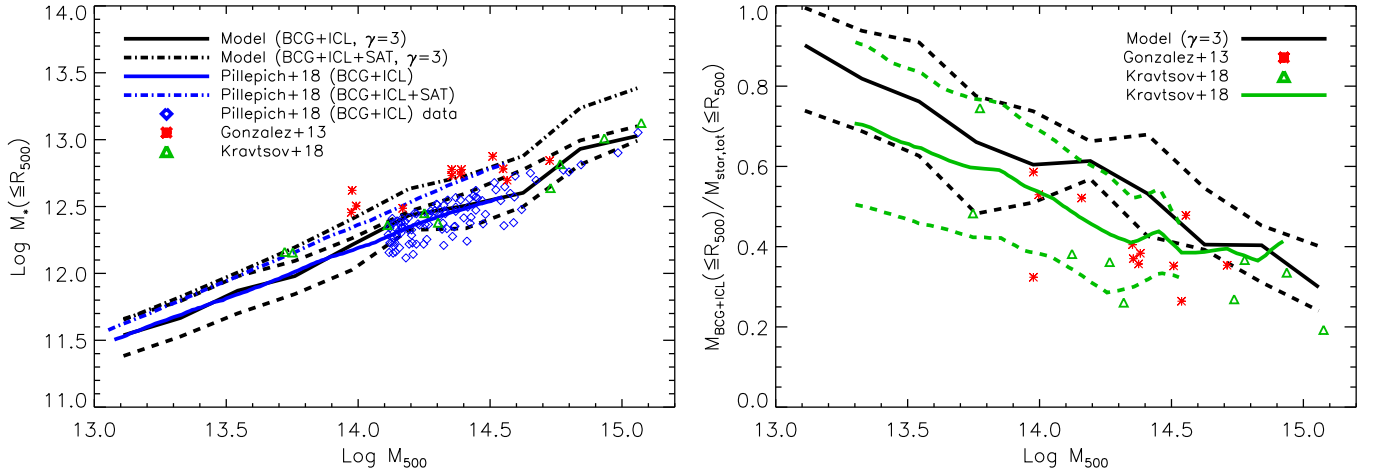


Figure 5. Left panel: mass of BCG+ICL (black solid line) and the same with the contribution of satellite galaxies (black dash-dotted line) within R_{500} as a function of the halo mass M_{500} compared with the simulations of Pillepich et al. (2018) and the observational data of Gonzalez et al. (2013) and Kravtsov et al. (2018). The amount of BCG+ICL within R_{500} is in perfect agreement with the simulated results (and so is the total stellar mass) and in good agreement with the observed ones (even though our prediction and the simulated data are systematically lower than the observed data by Gonzalez et al. (2013)). Right panel: the ratio within R_{500} between the BCG+ICL and total stellar mass as a function of the halo mass M_{500} , at redshift $z = 0$. The model prediction (black lines as in Figure 3) are compared with the sets of data by Gonzalez et al. (2013) and Kravtsov et al. (2018) as indicated in the legend. Overall, the observed trend is reproduced although our results appear to be biased with respect to the cloud of observed data. As highlighted in the text, there are caveats worth noting and they are fully discussed in Section 4.

The key point that comes from the comparison with both observed data and simulations at the present time (where data are supposed to be safer) is that our model is in better agreement with the observed data than the results of IllustrisTNG simulation. The predictions of Pillepich et al. (2018) are systematically higher than the data by DeMaio et al. (2020), because of a higher slope and similar intercept, and the widest gap is seen at high halo masses. Our ICL distribution is less concentrated toward the innermost regions than the simulated one, which translate into a lower amount of ICL in the central 100 kpc. In order to reach this conclusion, we developed a detailed analysis by comparing our predictions with IllustrisTNG’s results. We showed that both predict the same amount of BCG+ICL and BCG+ICL+satellite stellar mass within the clusters, and different amounts of ICL outside 100 kpc as a function of halo mass, that are separated by $1-\sigma$, with our predictions being higher than those of IllustrisTNG. Considering that our predictions better match the observed data, our profile gives a more accurate description of the ICL mass distribution within haloes, which is less concentrated than that invoked by Pillepich et al. (2018) (their equation 1). This statement has to be taken with caution and needs an explanation. Semi-analytic models, as reminded above, do not provide spatial information on the distribution of any component (while simulations do) and we obtained the distribution

of the ICL by assuming a NFW like profile with spherical symmetry. However, the fact that haloes of similar mass in Pillepich et al. have been stacked together with the assumption of spherical symmetry in order to get their functional form (their equation 1) makes the two models perfectly comparable in a statistical sense, and the differences in the results are not given by the assumption of spherical symmetry.

Moreover, as mentioned in Section 3, an important caveat must be discussed and concerns the definitions of the components considered. In fact, Pillepich et al. (2018) do not address the problem of splitting the BCG from the ICL, and call as “central”, i.e. BCG+(part of)ICL, all the stellar mass within a given aperture excluding the contribution from satellite galaxies. On the other hand, we are able to distinguish between the two components and our profile can perfectly isolate the amount of ICL within any given aperture. Since we assume that the BCG is confined within 100 kpc, the two definitions converge to the same (and so the problem drops) if in what they call “central”, the BCG stellar mass in their haloes is also confined within 100 kpc, which is likely the case for most of them.

In the last part of our analysis we tested our model against recent observed data by Gonzalez et al. (2013) and Kravtsov et al. (2018), at $z = 0$. We plot the amount of BCG and ICL, and that amount with the contribu-

tion of satellite galaxies within R_{500} , as a function of M_{500} , and the fraction of stellar mass in the BCG+ICL within R_{500} also as a function of M_{500} . In both cases we found a good agreement with the available observational data, although an important caveat is worth mentioning and discussing here and concerns the way the amount of BCG+ICL stellar mass has been computed observationally. [Gonzalez et al. \(2013\)](#) improved the measurements of the former data presented in [Gonzalez et al. \(2007\)](#) by using a fainter normalization when converting from magnitudes to luminosities that results in having luminosities (and so stellar masses) $\sim 15\%$ higher. In addition, when converting from luminosities to stellar masses, they also revisited the mass-to-light ratio used in [Gonzalez et al. \(2007\)](#). They considered a correction from dark matter estimated to be $\sim 15\%$, which results in a mass-to-light ratio about 26% lower than before, and by considering all corrections they found stellar masses around 13% lower. Then, with respect to their previous work, the revisited data in [Gonzalez et al. \(2013\)](#) are closer to our predictions.

Another important caveat must be mentioned and concerns both the comparison with [Gonzalez et al. \(2013\)](#) and [Kravtsov et al. \(2018\)](#), i.e. their definition of the ICL. [Kravtsov et al. \(2018\)](#) do not separate the BCG from its outer component (the ICL) and assume that the outer component can extend up to 200 kpc (270 and 340 kpc in two cases). They also note that in the sample of Gonzalez et al. the ICL is traced up to 300 kpc. This definition is not consistent with ours because our assumption is that the ICL extend over all the halo out to R_{200} . Although we did not show it, in the range of mass investigated by Gonzalez et al. and Kravtsov et al., according to our profile with $\gamma = 3$, the amount of ICL outside 300 kpc and within R_{500} can account from $\sim 15\%$ to $\sim 20\%$ of the total stellar mass. This means that, in the right panel of Figure 5, our predictions are somewhat higher than the observed data also because of the radial cut in measuring the ICL in the two observations.

The idea of describing the stellar mass distribution of the ICL through a modified version of the NFW profile for the dark matter is original, but recently there have been a few suggestions that the ICL could easily trace the dark matter distribution. [Montes & Trujillo \(2019\)](#) used a sample of six clusters from the Hubble Frontier Fields ([Lotz et al. 2017](#)) and compared the bi-dimensional distribution of the dark matter with that of the ICL by using the Modified Hausdorff distance (MHD). The MHD is a way of connecting the two distributions and quantifying their similarities and basically gives an idea of how far the two components are from each other (see their paper for further details). With that method they found that the average distance between ICL and dark matter is $\text{MHD} \sim 25\text{kpc}$ (within 140 kpc from the center), a result

which shows that the ICL follows the global dark matter distribution and can be used as a tracer of it. Similar conclusions have been taken by [Kluge et al. \(2020\)](#), who investigated on the ICL-cluster alignment with a sample of around 50 local clusters obtained with the Wendelstein Telescope Wide Field Imager. In order to qualify the ICL as a good tracer of the dark matter they examined four different criteria, including the ICL-cluster alignment, the BCG-cluster center offset and the ellipticity (the fourth criteria is the line of sight velocity). They concluded that the ICL is better aligned than the BCG with the host cluster in terms of both position and centering, making the ICL a better tracer of the dark matter than the BCG. Even more recently, [Alonso Asensio et al. \(2020\)](#) used the Cluster-EAGLE simulations ([Barnes et al. 2017](#); [Bahé et al. 2017](#)) to test the observational result of [Montes & Trujillo \(2019\)](#) quoted above. They used the same procedure used in Montes et al. and concluded that the stellar mass distribution follows that of the total (dark matter included), although their radial profiles differ substantially.

These results are not directly comparable with our predictions shown in Figure A6 and discussed in Appendix A since, in general, they differ in terms of method, redshift and halo mass range, but provide the hint that the ICL and the dark matter are really somewhat separated, and quantifying their separation in the next future with more observational data (by confirming the results of [Montes & Trujillo 2019](#) even at lower redshift) can be very useful in order to set the parameter γ of our model. Indeed, as already stated above, γ can be a function of halo properties such as the mass, or even redshift dependent, and also the only variable in the profile that accounts for the separation between the two components. We will aim to a detailed study on that when more observational data (that we can use to set the profile at different redshift and halo masses) are available.

5. CONCLUSIONS

We have taken advantage of a semi-analytic model of galaxy formation with a state-of-art implementation of the formation and evolution of the ICL to study its mass distribution along galaxy groups and clusters, in a wide range of halo mass and from redshift $z = 1.5$ to the present time. Given the fact that the semi-analytic model itself does not provide any spatial distribution, we have introduced a new profile for the ICL which is linked to that of the dark matter, motivated by recent observational and theoretical works. We have assumed that the ICL can be described by a simple NFW with a different concentration, which is coupled with that of the dark matter halo by the relation $c_{ICL} = \gamma c_{DM}$. By means of observational data of the $M_{100}^* - M_{500}$ relation (where M_{100}^* is the BCG+ICL stellar mass within 100

kpc and M_{500} the mass of the halo) at different redshifts, we have set the values of γ that best reproduced the observed data considered, and used those values to make a full comparison with other observational and theoretical works. From our analysis we can conclude the following:

- The fraction of BCG+ICL mass within the innermost 100 kpc is an increasing function of redshift and γ , and a decreasing function of the mass of the halo. This can be explained by the fact that less massive haloes are more concentrated and smaller than more massive ones, and that haloes of the same mass are, on average, less concentrated at higher redshift;
- The model is able to reproduce the $M_{100}^* - M_{500}$ relation with $\gamma = 3$ at the present time when compared with data by DeMaio et al. (2020), and closer than the prediction of IllustrisTNG (Pillepich et al. 2018) simulation. At higher redshift, the model prefers slightly higher values of γ and, despite it can reproduce the slope of the relation, especially at $z \sim 0.5$ it predicts an intercept that is lower than that found by DeMaio et al. by around 0.2 dex;
- A detailed comparison with the results of IllustrisTNG simulation shows that, although our predictions agrees very well in terms of amount or fraction of BCG+ICL (even including satellite galaxies) mass within R_{200} (in fairly good agreement with observational data either), the distributions of

the ICL along the halo are different. Our profile is less concentrated than that suggested by Pillepich et al. (2018), and this explains why our $M_{100}^* - M_{500}$ relation at the present time matches the observed one, while theirs is higher (similar intercept but a higher slope).

- By looking at the distance between the mass distributions of the ICL and the dark matter at $z = 0$ (see details in Appendix A), we find that low concentrated and more massive haloes have their dark matter and ICL distributions farther to each other than high concentrated and low mass haloes.

We suggest that a modified version of the NFW profile with a higher concentration can roughly describe the mass distribution of the ICL in wide ranges of halo mass and redshift. In order to better describe the ICL distribution in groups and clusters, more work is needed. The parameter γ that we have introduced, and that links the concentration of the ICL to the dark matter one, can be better constrained with the help of more observational data in a variety of redshifts. Our aim for a future work is to find the possible dependences of γ on halo mass and redshift, i.e a relation such as $\gamma = \gamma(M_{200}, z)$.

ACKNOWLEDGEMENTS

The authors thank the anonymous referee for his/her constructive comments which helped to improve the manuscript. This work is supported by the National Key Research and Development Program of China (No. 2017YFA0402703), and by the National Natural Science Foundation of China (Key Project No. 11733002).

APPENDIX

A. ICL AND DARK MATTER MASS DISTRIBUTIONS

We have linked the distribution of the ICL to the distribution of the dark matter through the concentration of the halo³, so it is natural to wonder how far the ICL and the dark matter mass distributions are from each other, assuming a given value of γ . We address this point in Figure A6, where we plot the distance (intended as the separation in kpc between the radii that enclose a given percentage of the mass of the two components, assuming spherical symmetry) between the two mass distributions, ICL and dark matter, as a function of the percentage of the total mass that the distributions consider, at $z = 0$. In the left panel we divide the full sample in three subsamples according to the concentration of the halo, from low ($c_{DM} < 4$) to high concentrations ($c_{DM} > 5$), while in the right panel we divide the sample in subsamples according to the halo mass, from low mass ($\log M_{200} < 13.5$) to high mass ($\log M_{200} > 14$). In both cases, the three subsamples have been chosen to have roughly the same number of haloes. The picture is that low concentrated haloes (red line in the left panel), which also roughly correspond to the most massive (red line in the right panel), have their dark matter and ICL distributions more distant with respect to high concentrated (green line in the left panel) and low mass (green line in the right panel) haloes. If we focus on the halo mass, which is a property of the halo that can be easily inferred, there is a remarkable difference in the distance of the two mass distributions between low mass haloes and high mass haloes. If we consider half of the mass distributions, in low mass haloes they are around 50 kpc distant, while in high mass haloes they are three times more distant, around 150 kpc. These results are qualitatively compared with other works and discussed in Section 4.

³ We remind the reader that $c_{ICL} = \gamma c_{DM}$.

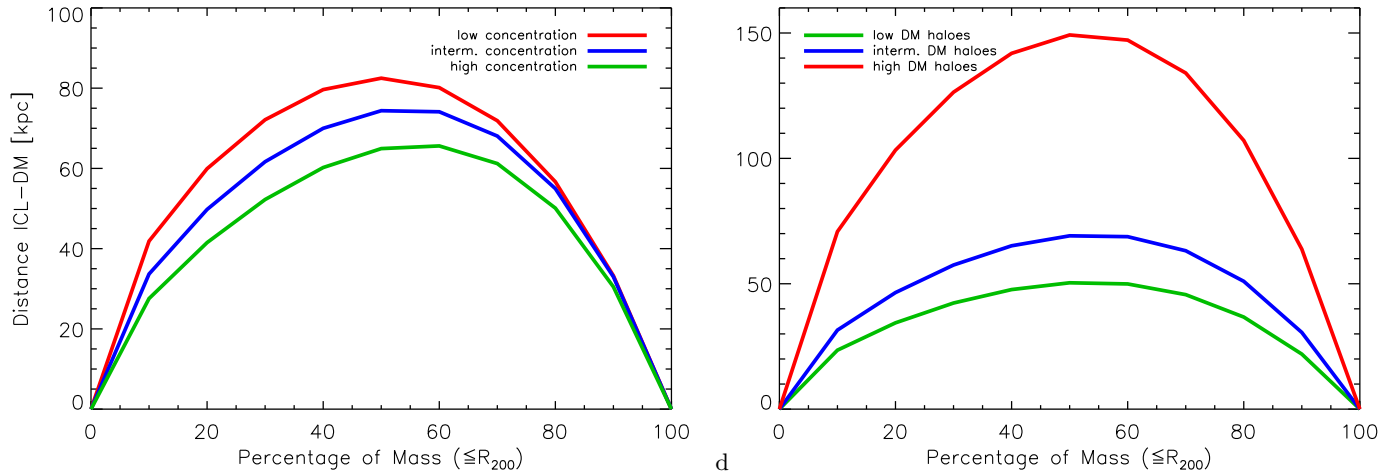


Figure A6: Distance between the mass distributions of dark matter and ICL as a function of the percentage of the total mass that the distributions consider, at $z = 0$. In the left panel our sample of haloes are divided according to their concentration, while in the right panel they are divided according to the halo mass. In both cases the sample has been split in order to have three subsamples with approximately the same number of objects (details are given in the text). Low concentrated haloes, which also correspond to the more massive, show to have their dark matter and ICL distributions more distant with respect to high concentrated and low mass haloes.

REFERENCES

- Alonso Asensio, I., Dalla Vecchia, C., Bahé, Y. M., et al. 2020, *MNRAS*, 494, 1859
- Bahé, Y. M., Barnes, D. J., Dalla Vecchia, C., et al. 2017, *MNRAS*, 470, 4186
- Barnes, D. J., Kay, S. T., Bahé, Y. M., et al. 2017, *MNRAS*, 471, 1088
- Burke, C., Hilton, M., & Collins, C. 2015, *MNRAS*, 449, 2353
- Chabrier, G. 2003, *PASP*, 115, 763
- Contini, E., De Lucia, G., & Borgani, S. 2012, *MNRAS*, 420, 2978
- Contini, E., De Lucia, G., Villalobos, Á., & Borgani, S. 2014, *MNRAS*, 437, 3787
- Contini, E., Yi, S. K., & Kang, X. 2018, *MNRAS*, 479, 932
- Contini, E., Yi, S. K., & Kang, X. 2019, *ApJ*, 871, 24
- De Lucia, G., & Blaizot, J. 2007, *MNRAS*, 375, 2
- DeMaio, T., Gonzalez, A. H., Zabludoff, A., Zaritsky, D., & Bradač, M. 2015, *MNRAS*, 448, 1162
- DeMaio, T., Gonzalez, A. H., Zabludoff, A., et al. 2018, *MNRAS*, 474, 3009
- DeMaio, T., Gonzalez, A. H., Zabludoff, A., et al. 2020, *MNRAS*, 491, 3751
- Gao, L., White, S. D. M., Jenkins, A., et al. 2004, *MNRAS*, 355, 819
- Gao, L., Frenk, C. S., Boylan-Kolchin, M., et al. 2011, *MNRAS*, 410, 2309
- Gonzalez, A. H., Zaritsky, D., & Zabludoff, A. I. 2007, *ApJ*, 666, 147
- Gonzalez, A. H., Sivanandam, S., Zabludoff, A. I., et al. 2013, *ApJ*, 778, 14
- Groenewald, D. N., Skelton, R. E., Gilbank, D. G., & Loubser, S. I. 2017, *MNRAS*, 467, 4101
- Han, S., Smith, R., Choi, H., et al. 2018, *ApJ*, 866, 78
- Iodice, E., Spavone, M., Cantiello, M., et al. 2017, *ApJ*, 851, 75
- Iodice, E., Spavone, M., Cattapan, A., et al. 2020, *A&A*, 635, A3
- Kluge, M., Neureiter, B., Riffeser, A., et al. 2020, *ApJS*, 247, 43
- Kravtsov, A. V., Vikhlinin, A. A., & Meshcheryakov, A. V. 2018, *Astronomy Letters*, 44, 8
- Lotz, J. M., Koekemoer, A., Coe, D., et al. 2017, *ApJ*, 837, 97
- Montes, M., & Trujillo, I. 2018, *MNRAS*, 474, 917
- Montes, M., & Trujillo, I. 2019, *MNRAS*, 482, 2838
- Morishita, T., Abramson, L. E., Treu, T., et al. 2017, *ApJ*, 846, 139
- Muldrew, S. I., Pearce, F. R., & Power, C. 2011, *MNRAS*, 410, 2617
- Murante, G., Giovalli, M., Gerhard, O., et al. 2007, *MNRAS*, 377, 2
- Navarro, J. F., Frenk, C. S., & White, S. D. M. 1997, *ApJ*, 490, 493
- Pillepich, A., Nelson, D., Hernquist, L., et al. 2018, *MNRAS*, 475, 648
- Prada, F., Klypin, A. A., Cuesta, A. J., et al. 2012, *MNRAS*, 423, 3018
- Presotto, V., Girardi, M., Nonino, M., et al. 2014, *A&A*, 565, A126
- Puchwein, E., Springel, V., Sijacki, D., & Dolag, K. 2010, *MNRAS*, 406, 936
- Purcell, C. W., Bullock, J. S., & Zentner, A. R. 2007, *ApJ*, 666, 20
- Rudick, C. S., Mihos, J. C., & McBride, C. K. 2011, *ApJ*, 732, 48
- Springel, V., White, S. D. M., Tormen, G., et al. 2001, *MNRAS*, 328, 726
- Springel, V. 2010, *MNRAS*, 401, 791
- Tang, L., Lin, W., Cui, W., et al. 2018, *ApJ*, 859, 85
- Zwicky, F. 1937, *ApJ*, 86, 217